

# Matter-wave frequency comb generation in dissipatively coupled microcavities

Seonghoon Kim<sup>1,\*</sup>, Yuri G. Rubo<sup>2</sup>, Timothy C. H. Liew<sup>3</sup>, Sebastian Brodbeck<sup>4</sup>, Christian Schneider<sup>4</sup>, Sven Höfling<sup>4,5</sup>, and Hui Deng<sup>6†</sup>

<sup>1</sup> *Department of Electrical Engineering and Computer Science,  
University of Michigan, Ann Arbor, MI 48109, USA*

<sup>2</sup> *Instituto de Energías Renovables, Universidad Nacional  
Autónoma de México, Temixco, Morelos 62580, Mexico*

<sup>3</sup> *Division of Physics and Applied Physics,  
School of Physical and Mathematical Sciences, Nanyang Technological University,  
21 Nanyang Link, Singapore 637371, Singapore*

<sup>4</sup> *Technische Physik, Universität Würzburg,  
Am Hubland, Würzburg 97074, Germany*

<sup>5</sup> *SUPA, School of Physics and Astronomy, University of St Andrews,  
St Andrews KY16 9SS, United Kingdom and*

<sup>6</sup> *Department of Physics, University of Michigan,  
450 Church Street, Ann Arbor, MI 48109, USA*

## Abstract

Optical frequency combs generated from mode-locked lasers have revolutionized high-precision metrology and spectroscopy [1, 2]. Recently, chip-scale and energy efficient micro-combs have been produced using microresonators [3–5] and quantum cascade lasers [6, 7] via cascaded four-wave mixing among the cavity modes. Here we report matter-wave frequency comb generation via a new physical mechanism in coupled exciton-polariton microcavities [8]. The interplay between the nonlinear polariton interaction and complex inter-cavity coupling leads to time-periodic modulation of the amplitudes and phases of the polariton condensate, forming a polariton frequency comb. Equidistant spectral lines are observed in photoluminescence and the first-order temporal coherence. The line spacing is determined by the interaction and coupling strengths, not the single-cavity modes. This new mechanism of comb generation allows non-resonant excitation with a power input much below the conventional semiconductor laser threshold. The comb line spacing is adjustable up to multi-terahertz frequency for a chip-scale low power terahertz source. The work opens a door to new phenomena and device applications of strongly nonlinear, coupled cavities.

---

\* shoon@umich.edu

† dengh@umich.edu

Semiconductor quantum-well microcavity exciton-polaritons are formed by strong coupling between excitons and photons in high quality cavities. They combine strong excitonic nonlinearity and robust long-range coherence in an open system [9, 10]. With recent developments in cavity engineering [11], we can now create multiple polariton sites with control over both the on-site interactions due to excitonic nonlinearities and inter-site coupling due to photon tunneling. Together with built-in interfaces for both electrical and optical integration, such coupled polariton cavities provide a promising platform for new phenomena and application of driven-dissipative, correlated quantum systems. Many phenomena characteristic of on-site interactions and Josephson coupling in matter-wave systems have been observed, such as Josephson oscillation [12], dynamical squeezing [13], and phase coupling [14]. Here, we report a phenomenon unique to open systems, resulting from dissipation induced coupling [8, 15]. We experimentally demonstrate that two polariton condensates in a microcavity are coupled both by Josephson tunneling and by radiative loss, leading to the formation of an equidistant polariton frequency comb.

When two polariton condensates are trapped close to each other, photon tunneling between them leads to Josephson coupling, resulting in the formation of bonding (B) and anti-bonding (A) states with split energies. Correspondingly, the radiation loss of the system is also modified, which can be described as dissipative coupling between the condensates, leading to different dissipation rates of the coupled states. The dissipation rate is higher (lower) when the two condensates are in-phase (out of phase) and emission from the condensates interfere constructively (destructively). Consequently, the total coupling becomes non-Hermitian. The interplay between polariton interactions and the non-Hermitian coupling between the condensates leads to a rich bifurcation diagram, as illustrated in Fig. 1a,b. The steady lasing states become unstable in the vicinity of condensation threshold and a limit-cycle solution emerges by critical Hopf bifurcation from the unstable single-mode lasing states [8], manifested as a polariton frequency comb with equidistantly spaced spectral lines.

The dynamics of such a coupled polariton system can be described by the driven-dissipative coupled polariton equation [8, 16]:

$$\frac{d\psi_{L,R}}{dt} = \frac{1}{2}(p_{L,R}\psi_{L,R} - \gamma\psi_{R,L} - \mu|\psi_{L,R}|^2\psi_{L,R}) - \frac{i}{2}(2\omega_{L,R}\psi_{L,R} - J\psi_{R,L} + \alpha|\psi_{L,R}|^2\psi_{L,R}). \quad (1)$$

Here  $\psi_{L,R}$  is the order parameter of the condensate in each site,  $\omega_{L,R}$  are the frequencies of the uncoupled cavity modes,  $p_{L,R} = P_{L,R} - \Gamma$  where  $P_{L,R}$  is the incoherent pump strength acting on site

$L, R$  and  $\Gamma$  is the cavity decay rate,  $\gamma$  is the dissipative coupling strength,  $\mu$  is the gain saturation parameter,  $J$  is the Josephson coupling strength, and  $\alpha$  is the on-site interaction strength. With a relatively strong on-site interaction and weak Josephson coupling (Fig. 1a), as  $P$  is varied, stable fixed-point and limit-cycle solutions, or a comb state, can exist between weak lasing in the anti-symmetrically coupled state and lasing in the symmetrically coupled state. For large  $J/\Gamma$  (Fig. 1b), the unstable fixed-point domain in the parameter space becomes small and requires large  $\gamma$  which may be difficult to realize. To realize the polariton comb, therefore, it is not always desirable to have a very high cavity quality factor, which increases  $J/\Gamma$ .

To establish the frequency comb, we use tightly confined, single-mode polariton condensates with controlled couplings. This is achieved with a GaAs-based microcavity with subwavelength grating (SWG) mirrors  $6\mu\text{m} \times 14\mu\text{m}$  in size, as illustrated in Fig. 1c [17]. Confinement and coupling of sites are controlled by both the lateral size and placements of the grating bars and the tethering pattern surrounding the SWG [18]. The tethering pattern controls the strain release when the sacrificial layer is removed and in turn controls the bending of the individual grating bars, as shown by simulations using COMSOL Multiphysics (Figure 1c). The bending of the SWG directly modulates the cavity length and thus the exciton-cavity detuning, through which we form a trapping potential for polaritons. Controlling the location and shape of the tethering patterns, therefore, controls both the height and width of the potential barrier between two sites. This tunability allows us to tune the three key cavity parameters that govern the many-body states of the system – the Josephson coupling strength  $J$ , dissipative coupling strength  $\gamma$ , and on-site interaction strength  $\alpha$ .

Figure 1d and e show the real-space and Fourier-space photoluminescence (PL) spectra of the polaritons at low pump powers. The states are discretized due to tight confinement, which also enhances the on-site interaction to on the order of  $10\text{ }\mu\text{eV}$  due to increased polariton density [19]. Bonding (B) and anti-bonding (A) states are formed due to Josephson coupling. Their separation gives the coupling strength  $J = 0.5\text{ meV}$ . The Josephson coupling decreases as the pump power increases because the pump spot is located at the center of the device where the potential barrier is (see Supplementary Figure S1 for the narrowing of energy separation between the bonding and anti-bonding states). The distance between the two minima of the effective potential is  $6.4\text{ }\mu\text{m}$ , corresponding to the separation of the two cavity sites. The next lowest energy state, labeled as state E in Figure 1, is formed from the first excited state of each uncoupled site at  $1.4\text{ meV}$  above

state A. This energy gap is much larger than the comb mode spacing for the system, therefore, the excited state within a single site does not affect the multi-frequency spectrum.

The transitions through the limit-cycle regime, as expected from equation (1), are clearly observed in the power dependence of the real-space spectra (Fig. 2). The PL spectrum at the low power (Fig. 1d,e) shows that the bonding state B initially has a larger population than the state A, because the pump spot is placed at the center of the device and prefers the B state.

As the pump power increases, the anti-bonding state A becomes more populated than state B (Fig. 2a, b, f). This corresponds to the onset of a weak lasing state at  $P = \Gamma - \gamma$ , where the system favors the state with the lowest decay rate[15]. The apparent asymmetry between the two sites is due to the symmetry breaking in the weak lasing regime [15]. Increasing power, bifurcation takes place and limit-cycle oscillations appear, leading to the appearance of new frequency components (Fig. 2c-d, g-h). We fit the spectrum of each site to equidistant Lorentzian lines. Above the bifurcation threshold, the right site R (red) consists of up to four equidistant lines, and the left site L (blue) up to three. At high pump powers, the PL eventually switches back to state B and other frequency components become insignificant, showing the system is transitional toward the single-mode B state lasing (Fig. 2e, h). (See supplementary information for the case when single-mode B state lasing is reached in the system.) This second transition takes place at  $P = \Gamma + 3\gamma$ . This sequence of transitions confirms dissipative coupling modeled by equation (1) and allows us to estimate the dissipative coupling rate for our system as  $\gamma = 0.055\text{ps}^{-1}$  (see Methods for details).

To verify the uniformity of the mode spacing, we measure the temporal first-order coherence  $g^{(1)}(\tau)$ , where multiple equidistant frequency lines would manifest as strong beating signals. On the R site, where four frequency components are present, more beating peaks are observed in  $g^{(1)}(\tau)$  compared to the L site. At low power, the beating signal is not well resolved due to the low coherence time (Fig. 3a). However, there exists a strong revival peak at 40 ps for both sites, which confirms there are multiple and equidistant frequency lines. As the populations in the two sites grow, the coherence time becomes longer, and the beating signal becomes more apparent (Fig. 3b). At higher power (Fig. 3c), the number of beating peaks and the complexity in  $g^{(1)}(\tau)$  decrease, suggesting the reduction of frequency components. We compare the experimental  $g^{(1)}(\tau)$  with computed results based on equation (1), as shown in Fig. 3d,e,f (see Methods for parameter values of the model). The simulation qualitatively captures the main features in experiment and shows similar beating peaks as in the experiment.

Finally, a hallmark of the limit-cycle states is a nontrivial relative phase  $\phi$  between the two sites. The dissipative coupling alone favors an out-of-phase relationship between the two sites with  $\phi = \pi$ . At the same time, on-site interaction changes the instantaneous frequency of each site. Interplay between these two interactions results in a nontrivial phase  $\phi \neq 0$  or  $\pi$  between the two sites when stable limit-cycle oscillations are formed. We measure the relative phase  $\phi$  by interfering both sites simultaneously with a reference beam and fit the interference fringes to obtain their phases [20]. As shown in figure 4, we obtain  $\phi = 0.51 \pm 0.08 \pi$  when the multiple frequency lines appear (Fig. 4a,d). When the B state brightens up at high powers, the relative phase changes to  $\phi = 0.21 \pm 0.06 \pi$  (Fig. 4b,e) and  $0.15 \pm 0.04 \pi$  (Fig. 4c,f), converging toward an in-phase relation for single-mode B state lasing. The above nontrivial phase relationship is also evidenced by the shift of the  $k = 0$  peak in the power-dependence of the k-space PL spectra as shown in the supplementary information.

In conclusion, we have demonstrated a new mechanism of frequency comb generation, resulting from dissipative coupling and nonlinear interactions in a coupled pair of polariton condensates. The equidistant frequency lines are measured spectrally and leads to coherence revivals in  $g^{(1)}(\tau)$ . The relative phase between the condensates is extracted from  $g^{(1)}(\tau)$  measurements; it decreases from  $\pi$  toward zero as the system transitions from unstable asymmetric lasing to limit-cycle to stable single-state lasing, which agrees very well with the theoretical prediction based on a model system of driven-dissipative equations for coupled polariton condensates (equation (1)). This excitation dependence of the polariton frequency comb confirms dissipative coupling between the condensates and provides an estimate of the dissipative coupling rate of about one tenth of the decay rate. A polariton-based frequency comb may allow very low input power, as it takes place near the polariton lasing threshold without electronic population inversion. It is also compatible with on-chip electrical excitation [21]. Future work to modify the quality factor and interaction strength of the microcavities may result in narrower linewidth of individual comb lines and greater line spacing up to terahertz frequencies.

## METHODS

**Sample.** Our microcavity sample is a  $\lambda/2$  AlAs cavity with three stacks of four GaAs quantum wells placed at the electric field maxima. The top mirror consists of high contrast subwavelength

grating and 2.5 pairs of  $\text{Al}_{0.15}\text{Ga}_{0.85}\text{As}/\text{AlAs}$  layers and the bottom mirror consists of 30 pairs of  $\text{Al}_{0.15}\text{Ga}_{0.85}\text{As}/\text{AlAs}$  layers. The Rabi splitting of 12 meV at 5 K was measured from the uncoupled single site. We designed various positions of the release patterns to control interactions between polaritons in the coupled cavities. The sample used in the main text has a center-to-center distance of  $6.4\ \mu\text{m}$  with  $6\ \mu\text{m}$  long grating bars. The length of the grating bar determines the size of the polariton mode in the single site and therefore controls the on-site interaction strengths. The center-to-center distance controls the Josephson and dissipative coupling strengths.

**Experimental set-up.** The microcavity sample is kept at 5 K in a closed-cycle cryostat. We use a continuous wave Ti:sapphire laser chopped with electro-optic modulator at 5 kHz with 5% duty cycle. The pump spot is focused on the center of the device with a diameter of  $2\ \mu\text{m}$ . We use a grating-based spectrometer and Michelson interferometer to resolve the spectral lines and beating peaks from these lines. For the measurement of  $\phi$ , we use the emission from one of the sites as a phase reference to determine the relative phase between the two sites, as the absolute phase of the polariton condensate is different for every experimental realization. We use a Mach-Zehnder interferometer and magnify the image from one arm by a factor of 6 compared to the other arm. For two spatial modes of  $2\ \mu\text{m}$  in diameter separated by  $7\ \mu\text{m}$ , magnification of about 4.5 is needed in order for the single-site to interfere with the entire system. Our magnification ensures that the two sites overlap with the center of the single-site where the phase is uniform. We fit interference pattern in each site to  $I_{L,R}(x) = I_{L,R}(x)(1 + |g_{L,R}^{(1)}|\cos(k_x x + \phi_{L,R}))$ , where  $I(x)$  is the Gaussian intensity profile,  $k_x$  is the spatial frequency of the fringe pattern due to the angle between two interfering beams. The relative phase is then calculated as  $|\phi_L - \phi_R|$ .

**Numerical simulations.** We numerically solved equation 1 using a fourth-order Adams-Bashforth-Moulton predictor-corrector method with small initial populations in both sites. Note that the initial condition does not affect the final state which converges to the limit-cycle solution. To account for the effect of noise, we multiplied exponential decay functions to the simulated  $g^{(1)}(\tau)$ . The parameters used for Fig. 3d,e,f were  $\Gamma = 0.5\ \text{ps}^{-1}$ ,  $\gamma = 0.077\ \text{ps}^{-1}$ ,  $\omega = 0$ ,  $J = 0.077\ \text{ps}^{-1}$ ,  $\alpha = 1.15\ \text{ps}^{-1}$ , and  $\mu = 0.015\ \text{ps}^{-1}$ . It is important to note that  $\alpha$  in the simulation is the polariton interaction strength multiplied by the polariton population. Considering the polariton population obtained experimentally, one requires polariton interaction strength to be an order of

10  $\mu\text{eV}$  which is in agreement with previous reports in GaAs polariton systems. We change the pumping strength  $P$  to account for the strength of the excitation power assuming other parameters do not change significantly above the lasing threshold. We used  $P = 0.524, 0.548, 0.627 \text{ ps}^{-1}$  respectively. We also gave 1% difference in pumping strength between two sites to account for the asymmetry in experiments.

The dissipative coupling strength can be estimated by the observed thresholds. It is convenient to express the equation (1) based on a pseudospin vector defined as  $\mathbf{S} = \frac{1}{2}(\Psi^\dagger \cdot \boldsymbol{\sigma} \cdot \Psi)$ , where  $\Psi = (\psi_1, \psi_2)^T$  and  $\boldsymbol{\sigma}$  is the Pauli vector.

$$\begin{aligned}\frac{dS_x}{dt} &= (p - \mu S)S_x - \gamma S - \alpha S_z S_y \\ \frac{dS_y}{dt} &= (p - \mu S)S_y + JS_z + \alpha S_z S_x \\ \frac{dS_z}{dt} &= (p - 2\mu S)S_z - JS_y \\ \frac{dS}{dt} &= (p - \mu S)S - \mu S_z^2 - \gamma S_x\end{aligned}$$

where  $S_x = \frac{1}{2}(\psi_2^* \psi_1 + \psi_1^* \psi_2)$ ,  $S_y = \frac{i}{2}(\psi_2^* \psi_1 - \psi_1^* \psi_2)$ ,  $S_z = \frac{1}{2}(|\psi_1|^2 - |\psi_2|^2)$ ,  $S = \frac{1}{2}(|\psi_1|^2 + |\psi_2|^2)$ . Then the nontrivial fixed point A state becomes stable when  $p = -\gamma$  and  $S_x = -S$ ,  $S_y = S_z = 0$ ,  $S = (\gamma + p)/\mu$ . This happened at the pump power of about 2 mW in the experiment (Fig 2b). The threshold for the stable fixed point B state is when  $p = 3\gamma$  and  $S_x = S$ . This corresponds to the pump power of about 3 mW when the system stabilized to the B state with weak satellite peaks (Fig 2e). Assuming  $\Gamma = 0.5 \text{ ps}^{-1}$  and  $P$  is a linear function of pump power, the estimated dissipative coupling strength is about  $0.055 \text{ ps}^{-1}$  which is reasonable considering the value we used for the simulation.

## ACKNOWLEDGMENT

S.K. and H.D. acknowledge the support by the National Science Foundation (NSF) under Awards DMR 1150593 and the Air Force Office of Scientific Research under Awards FA9550-15-1-0240. Y.G.R. acknowledges the support from CONACYT (Mexico) Grant No. 251808. T.L. was supported by the Ministry of Education (Singapore) grant 2017-T2-1-001. C.S., S.B. and S.H. acknowledge the support by State of Bavaria and the Deutsche Forschungsgemeinschaft (DFG) within the project SCHN11376 3-1. The fabrication of the SWG microcavities was performed in



the Lurie Nanofabrication Facility (LNF) at Michigan, which is part of the NSF NNIN network.

## REFERENCES

- [1] Udem, T., Holzwarth, R. & Hänsch, T. W. Optical frequency metrology **416**, 5 (2002).
- [2] Cundiff, S. T. & Ye, J. *Colloquium* : Femtosecond optical frequency combs. *Reviews of Modern Physics* **75**, 325–342 (2003). URL <https://link.aps.org/doi/10.1103/RevModPhys.75.325>.
- [3] Del’Haye, P. *et al.* Optical frequency comb generation from a monolithic microresonator. *Nature* **450**, 1214–1217 (2007). URL <http://www.nature.com.proxy.lib.umich.edu/nature/journal/v450/n7173/full/nature06401.html>.
- [4] Del’Haye, P. *et al.* Octave Spanning Tunable Frequency Comb from a Microresonator. *Physical Review Letters* **107** (2011). URL <https://link.aps.org/doi/10.1103/PhysRevLett.107.063901>.
- [5] Yao, B. *et al.* Gate-tunable frequency combs in graphenenitride microresonators. *Nature* **558**, 410–414 (2018). URL <http://www.nature.com/articles/s41586-018-0216-x>.
- [6] Hugi, A., Villares, G., Blaser, S., Liu, H. C. & Faist, J. Mid-infrared frequency comb based on a quantum cascade laser. *Nature* **492**, 229–233 (2012). URL <http://www.nature.com/doi/10.1038/nature11620>.
- [7] Kazakov, D. *et al.* Self-starting harmonic frequency comb generation in a quantum cascade laser. *Nature Photonics* **11**, 789 (2017). URL <http://www.nature.com/articles/s41566-017-0026-y>.
- [8] Rayanov, K., Altshuler, B., Rubo, Y. & Flach, S. Frequency Combs with Weakly Lasing Exciton-Polariton Condensates. *Physical Review Letters* **114**, 193901 (2015). URL <http://link.aps.org/doi/10.1103/PhysRevLett.114.193901>.
- [9] Deng, H., Haug, H. & Yamamoto, Y. Exciton-polariton Bose-Einstein condensation. *Reviews of Modern Physics* **82**, 1489–1537 (2010). URL <http://link.aps.org/doi/10.1103/RevModPhys.82.1489>.
- [10] Carusotto, I. & Ciuti, C. Quantum fluids of light. *Reviews of Modern Physics* **85**, 299–366 (2013). URL <http://link.aps.org/doi/10.1103/RevModPhys.85.299>.

- [11] Schneider, C. *et al.* Exciton-polariton trapping and potential landscape engineering. *Reports on Progress in Physics* **80**, 016503 (2017). URL <http://stacks.iop.org/0034-4885/80/i=1/a=016503>.
- [12] Abbarchi, M. *et al.* Macroscopic quantum self-trapping and Josephson oscillations of exciton polaritons. *Nature Physics* **9**, 275–279 (2013). URL <http://www.nature.com.proxy.lib.umich.edu/nphys/journal/v9/n5/full/nphys2609.html>.
- [13] Adiyatullin, A. F. *et al.* Periodic squeezing in a polariton Josephson junction. *Nature Communications* **8**, 1329 (2017). URL <http://www.nature.com/articles/s41467-017-01331-8>.
- [14] Ohadi, H. *et al.* Nontrivial Phase Coupling in Polariton Multiplets. *Physical Review X* **6** (2016). URL <https://link.aps.org/doi/10.1103/PhysRevX.6.031032>.
- [15] Aleiner, I. L., Altshuler, B. L. & Rubo, Y. G. Radiative coupling and weak lasing of exciton-polariton condensates. *Physical Review B* **85**, 121301 (2012). URL <http://link.aps.org/doi/10.1103/PhysRevB.85.121301>.
- [16] Ohadi, H. *et al.* Spontaneous Spin Bifurcations and Ferromagnetic Phase Transitions in a Spinor Exciton-Polariton Condensate. *Physical Review X* **5**, 031002 (2015). URL <http://link.aps.org/doi/10.1103/PhysRevX.5.031002>.
- [17] Zhang, B. *et al.* Zero-dimensional polariton laser in a subwavelength grating-based vertical microcavity. *Light: Science & Applications* **3**, e135 (2014). URL <http://www.nature.com.proxy.lib.umich.edu/lsa/journal/v3/n1/full/lsa201416a.html>.
- [18] Zhang, B. *et al.* Coupling polariton quantum boxes in sub-wavelength grating microcavities. *Applied Physics Letters* **106**, 051104 (2015). URL <http://scitation.aip.org.proxy.lib.umich.edu/content/aip/journal/apl/106/5/10.1063/1.4907606>.
- [19] Kim, S. *et al.* Coherent Polariton Laser. *Physical Review X* **6**, 011026 (2016). URL <http://link.aps.org/doi/10.1103/PhysRevX.6.011026>.
- [20] Manni, F., Lagoudakis, K. G., Liew, T. C. H., André, R. & Deveaud-Plédran, B. Spontaneous Pattern Formation in a Polariton Condensate. *Physical Review Letters* **107**, 106401 (2011). URL <http://link.aps.org/doi/10.1103/PhysRevLett.107.106401>.
- [21] Suchomel, H. *et al.* An electrically pumped polaritonic lattice simulator. *arXiv:1803.08306 [physics]* (2018). URL <http://arxiv.org/abs/1803.08306>. ArXiv: 1803.08306.

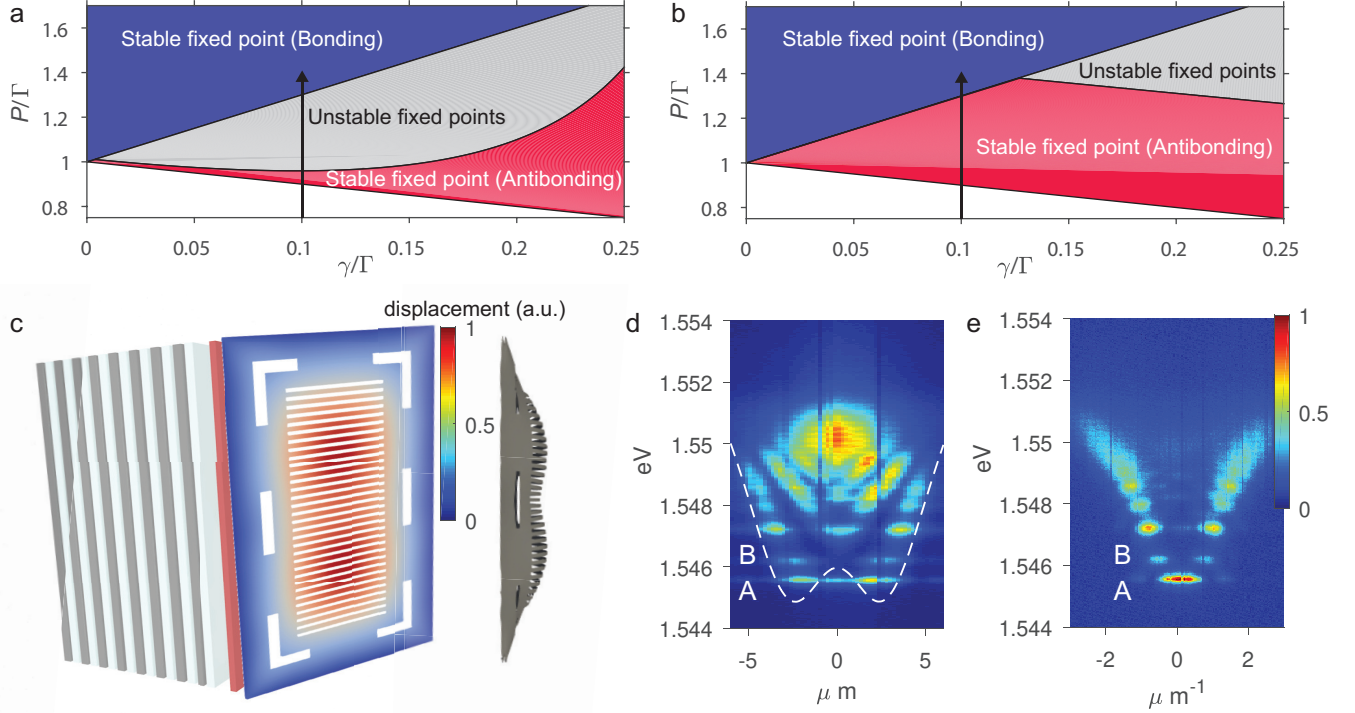


FIG. 1: Bifurcation diagram and the sample properties at low excitation powers. a,b, Bifurcation diagram of equation (1) in  $P - \gamma$  parameter space for  $J/\Gamma = 0.07, 2.5$ , respectively. Other parameters are  $\alpha/\Gamma = 0.25$ ,  $\mu/\Gamma = 0.05$  for both diagrams. A standard lasing threshold is when  $P = \Gamma$  in the absence of dissipative coupling. For certain values of  $\gamma > 0$ , thresholds for stable and unstable fixed-point solutions emerge as  $P$  increases, indicated by arrows for  $\gamma/\Gamma = 0.1$ . c, A schematic of the sample structure with a bent SWG mirror. Bending of the SWG is simulated by COMSOL and shown both by the color map in the schematic view and in the side view. The bending is less where there are open slots in the tethering pattern and vice versa. d, The real-space photoluminescence (PL) spectrum of the coupled polariton system showing the discrete polariton states at low excitation powers. The ground state is formed by the bonding state (B state), while the first excited state is the anti-bonding state (A state). The white dashed line illustrates the potential due to the bending of the SWG shown in c. e, The corresponding Fourier space spectrum showing the B state at  $k = 0$  and the A state at  $k = \pm\pi/a$ , where  $a$  is the distance between the two coupled sites.

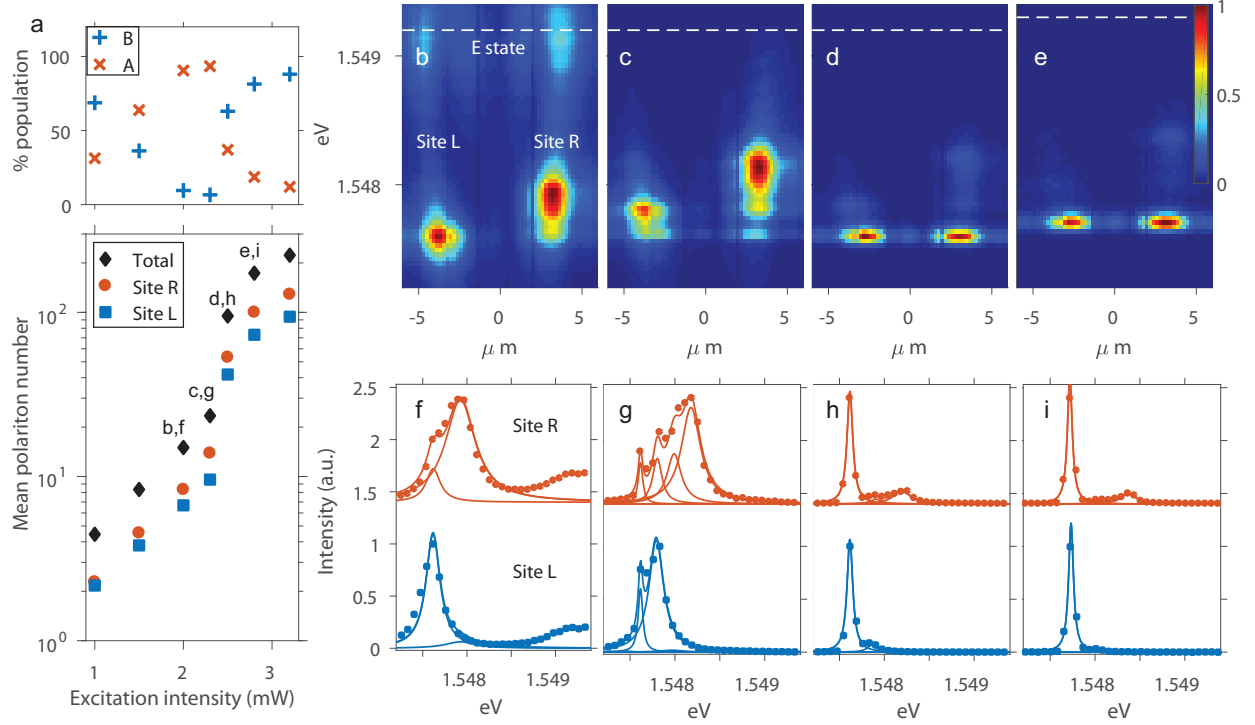


FIG. 2: Excitation power dependence of the intensity and real-space spectra of the polariton PL near the A and B states. a, Bottom: Mean polariton number of the A and B states vs. the excitation power for the L site (blue square), R site (red circle) and the sum of the L and R sites (black diamond). It shows clearly a threshold behavior and degenerate occupation at each site. Top: Relative fraction of the B state (blue plus) and A state (red cross) population vs. the excitation power, showing switching of the dominant state upon transitions to the A-state weak lasing and stable B-state lasing. b-e, The real-space spectra at four different excitation powers, showing the transition from A state weak lasing, to limited cycles, toward B state lasing. The white dashed line marks the E state – the lowest energy state after B and A states. f-i, Spectrum of each site obtained from b-e respectively. The solid lines are fits by equidistant Lorentzians. More than two frequency components are apparent in c, d, g & h.

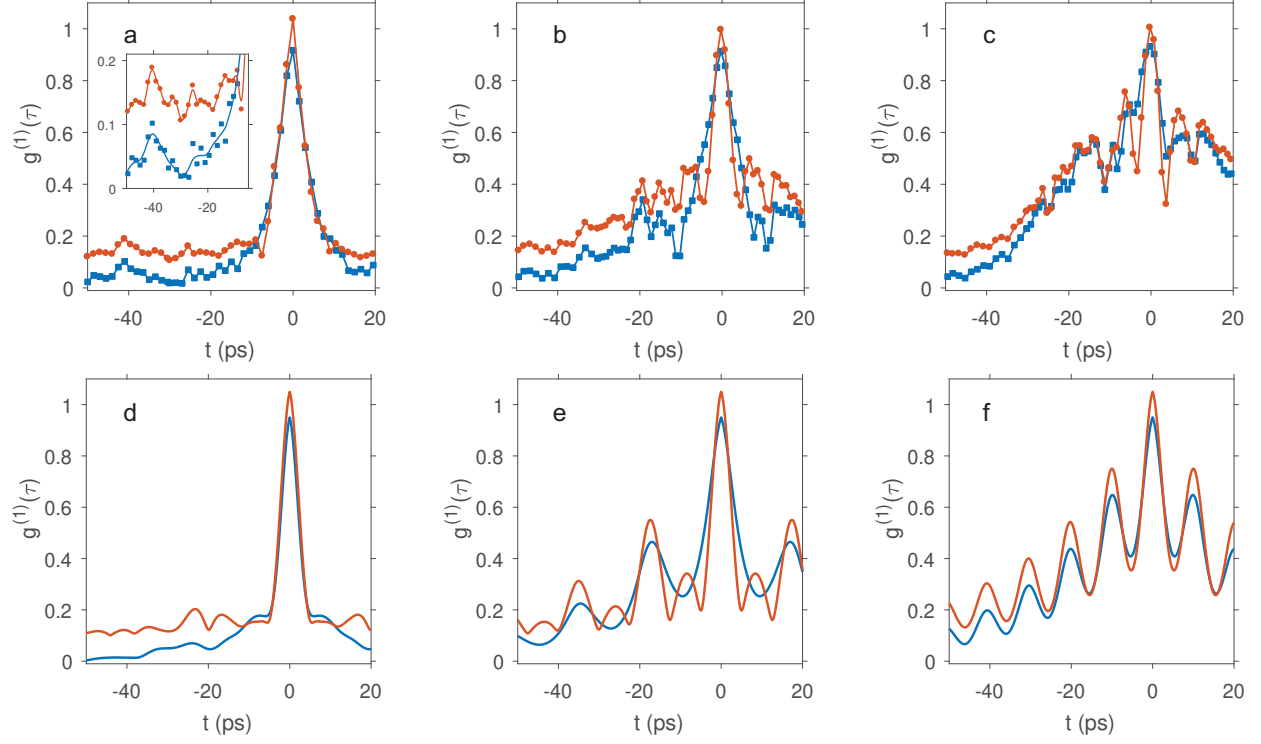


FIG. 3: Experimental (a-c) and theoretical (d-f)  $g^{(1)}(\tau)$  for three different excitation powers, corresponding to Fig. 2c-e, respectively. Red dots are shifted vertically by 0.1 for better visibility. The inset shows a zoom in of the beating peaks in a (The lines are guides to the eye). The site with more frequency lines has more beating peaks and narrower  $g^{(1)}(\tau)$  linewidths at  $t=0$ . The simulated  $g^{(1)}(\tau)$  is multiplied by an exponential decay with decay times of 20, 25, 30 ps respectively.

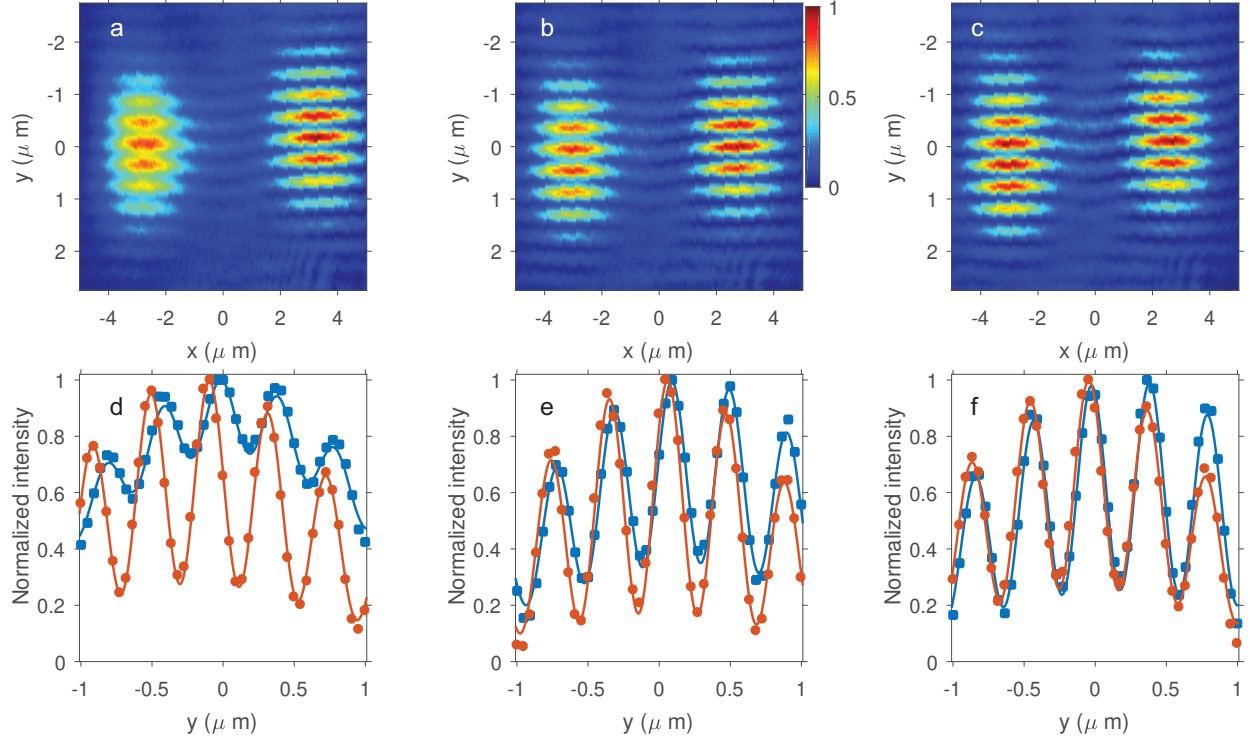


FIG. 4: Relative phase measurement between L and R sites at excitation powers of 2 mW (a,d), 2.3 mW (b,e) and 2.5 mW (c,f). a-c, Interference images from interfering both sites to a magnified single site. d-f, Interference fringes for each site obtained from a-c along  $x = \pm 3 \mu\text{m}$  (dots). The solid lines are fits as described in Methods. From the fit, we obtain the relative phase difference of  $0.51 \pi$ ,  $0.21 \pi$ , and  $0.15 \pi$  respectively.